nature catalysis

Article

https://doi.org/10.1038/s41929-024-01205-5

Atomically dispersed ruthenium hydride on beta zeolite as catalysts for the isomerization of muconates

Received: 18 July 2022

Accepted: 12 July 2024

Published online: 19 August 2024

Check for updates

Ibrahim Khalil[1], Marco Giulio Rigamonti[1], Kwinten Janssens[2], Aram Bugaev[3], Daniel Arenas Esteban[4], Sven Robijns[1], Thibaut Donckels[1], Mostafa Torka Beydokhti[1], Sara Bals[4], Dirk De Vos[2] & Michiel Dusselier[1]

Searching for sustainable polymers requires access to biomass-based monomers. In that sense, glucose-derived *cis*,*cis*-muconic acid stands as a high-potential intermediate. However, to unlock its potential, an isomerization to the value-added *trans*,*trans*-isomer, *trans*,*trans*-muconic acid, is required. Here we develop atomically dispersed low-loaded Ru on beta zeolite catalysts that produce *trans*,*trans*-muconate in ethanol with total conversion (to equilibrium) and a selectivity of >95%. We reach very high turnovers per Ru and productivity rates of 427 mM h^{-1} (~85 g l^{-1} h^{-1}), surpassing the bio-based *cis*,*cis*-muconic acid production rates by an order of magnitude. By coupling isomerization to Diels–Alder cycloaddition, terephthalate intermediates are produced in around 90% yields, circumventing the isomer equilibrium. Isomerization is promoted by Ru hydride species where the hydrides are generated from the alcohol solvent, as evidenced by Fourier transform infrared spectroscopy. Beyond isomerization, the Ru–zeolite and its hydride-forming capacity could be of use as a heterogeneous catalyst for other hydride chemistries, demonstrated by a successful hydride transfer hydrogenation.

In a future circular economy, renewable carbon should make up for losses in recycling loops[1]. Next to CO_2-based routes, biomass-based (photosynthetically fixed CO_2) production paths to chemicals will be essential to counter the environmental issues with the use of petroleum-based feedstocks[2,3]. Attempts to produce value-added molecules and building blocks from biomass have notably evolved in recent years[4–6]. For the production of aromatics, phenolics and certain olefins, lignin appears to be a good candidate[7–9]. To obtain functional molecules with carboxylic and/or alcoholic groups (and low C/O ratios), glucose derived from cellulosic biomass is the most promising starting material as this allows one to aim for high atom economy—as opposed to processing glucose into deoxygenated products[10,11]. Both chemocatalytic and biotechnological processes have been reported to provide access to platform molecules and building blocks from hexoses or pentoses, for example, lactic acid[4,12], maleic acid[13,14] and levulinic acid[15,16]. Combining the two approaches grants access to more diverse compounds via the biological conversion of biomass derivatives by engineered micro-organisms into platforms that are further transformed by chemical catalysis into desired chemicals[17–19]. Muconic acid (MA) is a good example of a biotech-made platform molecule, which can lead to a range of valuable derivatives (for example, adipic acid, terephthalic acid and ε-caprolactam), or serve directly as a bulk (co-)

[1]Center for Sustainable Catalysis and Engineering (CSCE), KU Leuven, Leuven, Belgium. [2]Centre for Membrane Separations, Adsorption Catalysis and Spectroscopy for Sustainable Solutions (cMACS), KU Leuven, Leuven, Belgium. [3]Paul Scherrer Institut, Villigen, Switzerland. [4]Electron Microscopy for Materials Science (EMAT) and NANOlab Center of Excellence, University of Antwerp, Antwerp, Belgium. e-mail: michiel.dusselier@kuleuven.be

https://doi.org/10.1038/s41929-024-01205-5

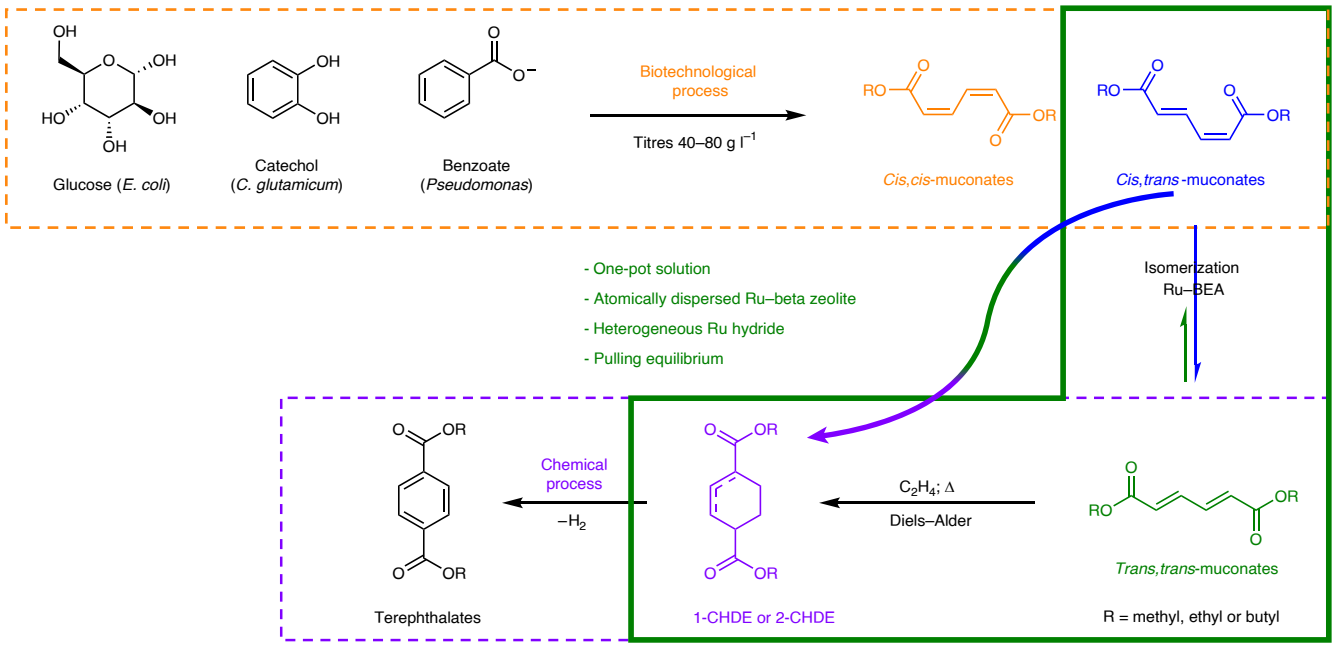

Fig. 1 | Valorization route of *ct*-muconates from the tandem isomerization and Diels–Alder reactions. The current bio-based and biochemical routes to produce *cis*,*cis*- and *cis*,*trans* isomers (orange), and chemical transformation of *trans*,*trans*-isomer into terephthalates (purple). The proposed one-pot transformation of *ct*-muconate into CHDE is shown in the green box. The tandem isomerization and Diels–Alder reactions are performed in the presence of Ru hydride on beta zeolite and ethylene to yield CHDE (an intermediate of terephthalates). *E. coli*, *Escherichia coli*; *C. glutamicum*, *Corynebacterium glutamicum*; BEA, beta zeolite; Δ, symbol for heat.

monomer in polymers[20–26]. The diacid owns a diene functionality, and thus MA has three isomeric forms: *cis*,*cis*-MA (*cc*-MA) and *cis*,*trans*-MA (*ct*-MA), both industrially produced in the biochemical fermentation of glucose[27], and the most valuable *trans*,*trans*-MA (*tt*-MA), which can be accessed only by isomerization of *cc*-MA or *ct*-MA or via a complex lab-scale chemical synthesis[20,28,29]. A full overview of routes to and from MA can be found in our review[20]. The added value of *tt*-MA is explained by its unique potential as a monomer in polymerization as well as by its reactivity towards Diels–Alder cycloaddition to yield the partially hydrogenated terephthalic acid precursors: tetrahydrohydroterephthalic acid isomers (Fig. 1)[30–32]. These precursors can be dehydrogenated into terephthalic acid or even used as co-monomers for specialty polymers[24,31,33–35]. To date, the most prominent isomerization route to *tt*-MA uses homogeneous iodine (I_2) under UV light[36]. This photochemical inversion was first reported by Grundmann in 1936 (ref. 36); however, the mechanism was only recently described by Settle et al. as a reversible addition of iodine radicals on the double bonds of MA[37]. Despite the high rates, the industrial application of the I_2/UV process is hindered by the high corrosiveness of iodine, which restricts its use at high concentrations[20,31,38]. Alternative isomerization systems have been reported but none of these translate to large-scale *tt*-MA production due to limitations such as relatively high cost for few turnovers (5% Pd/C catalyst), the catalyst recovery and regeneration, or *tt*-MA isolation (homogeneous catalysts, sacrificial reagents or viscous solvents)[31,34,39–41]. The search for an affordable, productive and more sustainable isomerization leads us to propose a heterogeneously catalysed conversion of *cc*- and *ct*-muconic esters using Ru–zeolites. The choice of zeolites is due to their low cost, their ability to host metals and their thermal stability[42–44], whereas the choice for Ru as the diene isomerization catalyst was inspired by its reported activity in the homogeneous and heterogeneous isomerization of olefins (for example, in linoleic acid where conjugated bonds form)[45,46]. Since Ru is a rare transition metal, preparing a heterogeneous catalyst that features atomically dispersed ionic Ru atoms with high activity (to maximize the atom utilization efficiency) is of great interest, not only for isomerization[47,48].

In this work we show that beta zeolites with 0.2 wt% atomically dispersed Ru are highly active for the production of *tt*-muconate (>300 mM h^{-1}) in around 70% yield, that is, right up to the thermodynamic equilibrium between *ct* and *tt*, with selectivity surpassing 95%. Muconic esters (muconates) were used rather than MA due to their capacity to avoid intramolecular lactonization, as proven in an earlier report[41], although a direct esterification–isomerization on the acid feedstock was also proven to work. When coupled to the Diels–Alder reaction (Fig. 1), the consumption of *tt*-isomer breaks the thermodynamic equilibrium of the isomerization, thus leading to the Diels–Alder product (a tetrahydrohydroterephthalate, here called cyclohexene-1,4-dicarboxylic acid diester (CHDE)). The mechanistic studies show that the isomerization proceeds via a Ru hydride mechanism, where the hydride is generated from the alcohol, which was proven with elaborated mechanistic studies, including experimental tests with isotopically labelled molecules followed by NMR and Fourier transform infrared (FT-IR) spectroscopy methods. In addition, a preliminary techno-economic analysis was performed to estimate the potential relevance of our process. Finally, the newly designed Ru hydride catalysts are shown to have promise for other applications, such as a hydride transfer hydrogenation tested on three different substrates.

Results

Muconic acid versus muconates as feedstocks

In most previously reported pathways (except with I_2)[37], the formation of *tt*-MA from *cc*-MA proceeds via *ct*-MA[20], and this first isomerization was shown to occur in water (or to be assisted by water; activation energy, E_a = 76 kJ mol^{-1}), occurring already at 25 °C when pH < 4 (refs. 31,49). The second isomerization is kinetically hindered: no *tt*-MA is observed even after heating to 75 °C (Supplementary Fig. 1a). Instead, intramolecular reactions lead to undesired mono- and di-muconolactones (Supplementary Fig. 1d). In addition, the low solubility of MA isomers in water (~1 g l^{-1} for *cc*-MA at 15 °C) prevents upscaling. Higher solubility is found in alcohols (for example, ~28 g l^{-1} in ethanol)[20]. Favourably,

https://doi.org/10.1038/s41929-024-01205-5

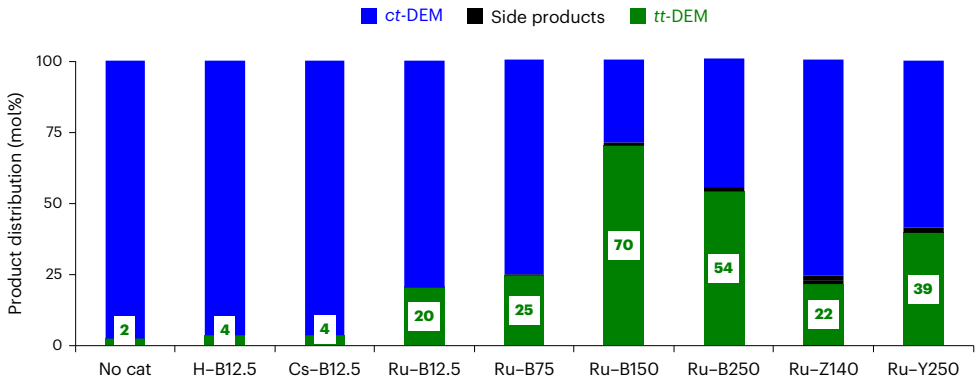

Fig. 2 | Proof of concept of the isomerization of muconates over several Ru-loaded zeolites. The product distribution (mol%) in the isomerization of *ct*-DEM into *tt*-DEM performed on a selection of Ru-containing zeolites (with and without 0.2 wt% Ru). Conditions are as follows: 50 mg catalyst (activated at 350 °C under N_2 flow) + 30 mM *ct*-DEM in 5 ml ethanol at 130 °C and 14 bar N_2 for 2 h. No cat, no catalyst added; H, Cs or Ru is the exchanged ion; B, beta, Z, ZSM-5; Y, USY zeolite; numbers next to the topology code refer to the respective Si/Al ratio of the zeolites.

ethanol promotes the second isomerization reaction, yielding 11% *tt*-MA (versus 0% in water) after 120 h; however, ethanol slows the initial isomerization kinetics, requiring 40 h to reach full conversion of *cc*-MA (instead of 0.5 h in water; Supplementary Fig. 1a,b). Despite the good MA solubility in ethanol and the formation of *tt*-MA (11%), lactonization was still favoured (19% of mono-muconolactone).

To avoid lactonization, the carboxylic functionalities were protected by esterification, and alkyl muconates were prepared (*ct*-dimethyl muconate, *ct*-DMM; *ct*-diethyl muconate, *ct*-DEM; and *ct*-dibutyl muconate, *ct*-DBM). Muconates are used as monomers for polymuconates or as platform molecules for terephthalates and adipates[20,30,37]. They also present higher solubility in organic phases (for example, *ct*-DEM is miscible with ethanol)[20], which could allow high productivities in an isomerization process, possibly surpassing the biotechnological production rate of MA. Lactonization was effectively eliminated, but the spontaneous isomerization of the muconate in ethanol was also found to be absent (Supplementary Fig. 1c, dashed lines). This is due to the higher energy barrier in comparison to the one for acid (210 kJ mol^{-1} for *cc*-DMM to *ct*-DMM versus 76 kJ mol^{-1} for *cc*-MA to *ct*-MA)[31,37], highlighting the need for a catalyst, especially when aiming for the *tt*-isomer, which presents an even higher energy barrier of about 270 kJ mol^{-1} (*ct*-DMM to *tt*-DMM)[37]. The addition of a Ru-exchanged zeolite to the ester in ethanol solution gave the first proof of the catalytic capability of Ru in the formation of the *tt*-isomer, with around 30% *tt*-DEM formed at 75 °C after 120 h at 100% selectivity (Supplementary Fig. 1c, solid lines and histogram). The Ru-exchanged zeolite was also capable of catalysing the formation of *tt*-MA; however, the limitations of low solubility and the competitive lactonization persisted.

Catalyst preparation and investigation of Ru active species

Optimizing the Ru loading method to achieve atomic dispersion and studying the role of the activation conditions is key to avoiding Ru sintering and achieving the atomically dispersed Ru on zeolite catalysts with the desired isomerization activity[48,50]. First, Ru was loaded by ion exchanging $Ru(NH_3)_6Cl_3$ on caesium-exchanged zeolites, which were obtained following the procedure described in Methods. The effect of the type of pre-cation on the final Ru loading on the zeolite is investigated in Supplementary Table 1. Neither H^+-exchanged nor Cs^+-exchanged zeolite showed activity in comparison to the blank (Fig. 2). To ensure the high Ru dispersion, the amount of added Ru was lower than (or equal to) the amount of strong Brønsted acid sites estimated by pyridine adsorption followed by infrared spectroscopy (Supplementary Table 2). Due to the large pore size and availability in various Si/Al ratios (B*x*, where *x* refers to the respective Si/Al ratio), beta zeolites were first selected to host 0.2 wt% Ru (Fig. 2). After 2 h, some formation of *tt*-DEM was noticed with Ru–B12.5 and Ru–B75 (20 mol% and 25 mol%, respectively). Ru–B150 was the most active, reaching 70% yield of *tt*-DEM. The lower activity observed on Ru–B12.5 and Ru–B75 catalysts may be due to residual large Cs^+ cations, which can slow the diffusion of the reagents towards the Ru sites by a steric effect or physical interactions (as shown in Supplementary Fig. 2 for the strong adsorption of methanol over the Cs-exchanged zeolite). Also, the location of the hosting sites for Ru (strong zeolite acidic sites) could also play a role in defining the rate of the isomerization. With a higher Si/Al ratio (Ru–B250), only 0.16 wt% Ru could be loaded, which may be the reason for the slightly lower *tt*-DEM formation within the same reaction time (54% yield but comparable turnover frequency as for Ru–B150). With an extended reaction time, 70% *tt*-DEM can be produced over all beta zeolites, which equals the thermodynamic equilibrium that prevents further *tt* formation[34]. To validate this experimental finding, the equilibrium between *ct*- and *tt*-hexa-2,4-diene was simulated in a thermodynamic model, and indeed at 130 °C the *tt*-isomer constitutes 77% of the mixture, while higher temperatures favour the formation of *ct*-isomer (Supplementary Fig. 3). The reverse isomerization, from *tt* to *ct*, was also observed when starting with a solution of *tt*-DEM (17% *ct*-DEM within 2 h at 130 °C). Other zeolite topologies with high Si/Al ratios, for example Zeolite Socony Mobil–5 (ZSM-5; framework type MFI, Si/Al = 140) and ultrastable zeolite Y (USY; faujasite (FAU)-type, Si/Al = 250) were loaded with 0.2 wt% Ru and only 22% and 39% *tt*-DEM formed, respectively (Fig. 2). For the medium-pore ZSM-5, the smaller pores likely limit the access towards the Ru sites. The lesser performance of USY250 (versus siliceous beta) could be linked to the lower stability of Ru species in USY250, which showed leaching during the reaction. In addition, Ru loading was increased on B150 (from 0.2 wt% to 0.4 wt%) leading to a rather limited increase in the *ct*-DEM conversion rate (from 3.0 mmol g_{zeo}^{-1} h^{-1} to 3.9 mmol g_{zeo}^{-1} h^{-1}; g_{zeo}, 1 gram of zeolite) at the expense of a lower selectivity (94% versus 73%) due to the formation of a mono-hydrogenated by-product (Supplementary Figs. 4 and 5). As a result of this dilute regime screening, 0.2%Ru–B150 is clearly the most suitable catalyst for the isomerization of muconic esters.

The activation conditions were crucial to maintain Ru in an atomically dispersed, active state (all previous catalysts were activated at 350 °C under N_2 flow). The as-made 0.2%Ru–B150 catalyst (no activation) shows the formation of only 22% *tt*-DEM from 23% *ct*-DEM within 1.5 h at 150 °C (Supplementary Table 3). Increasing yields of *tt*-DEM were observed when activating the catalyst at 120 °C and 200 °C: 35% and 66%, respectively. Activation at 250 °C, 300 °C or 350 °C (under N_2 flow) leads to the highest yields of *tt*-DEM (69–71%) at 72–75% *ct*-DEM conversion, which is the thermodynamic equilibrium. A higher activation

https://doi.org/10.1038/s41929-024-01205-5

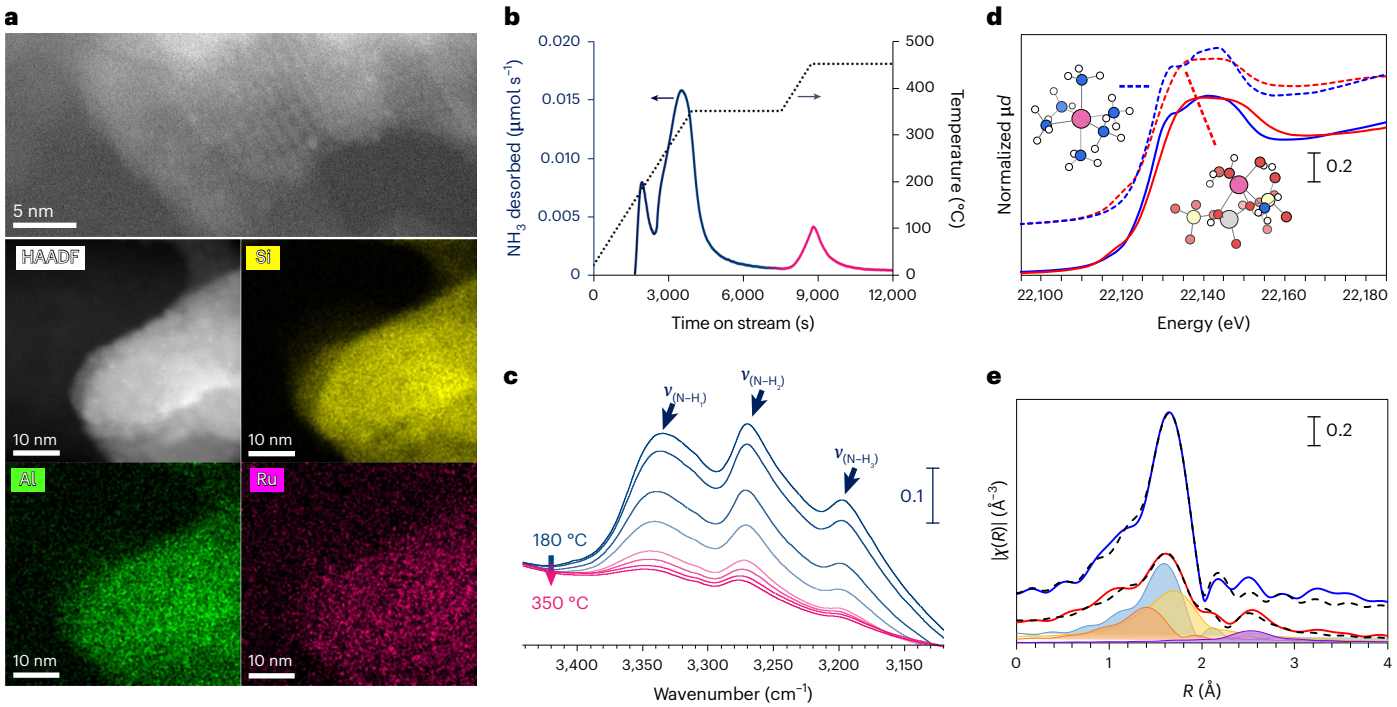

Fig. 3 | Characterization and proposition of the Ru complex in beta zeolite. **a**, High-resolution HAADF-STEM image of an area where bright spots can be observed within the zeolite pore structure (5 nm image) and EDS map (10 nm image) of 0.2%Ru–B150 catalyst after activation. **b**,**c**, Temperature-programmed desorption of NH_3 ligands (5 °C min^{-1}) from 0.2%Ru–B150 catalyst followed by mass spectrometry and FT-IR spectroscopy (**c**). $\nu_{(N-Hx)}$ refers to the three different stretching vibrations of nitrogen-hydrogen bonds in the NH_3 ligands. The vertical scale is presented in an arbitrary unit. **d**, The normalized XANES absorbance (μ*d* in arbitrary unit, vertical scale) as a function of the energy (eV) for the tested $Ru(NH_3)_6Cl_3$ (solid blue) and activated 0.2%Ru–B150 catalyst (solid red) in comparison with simulated XANES (dashed lines) for the proposed atomic models shown as insets (colour code: purple, Ru; blue, N; white, H; red, O; yellow, Si; grey, Al). **e**, Magnitude of the experimental Fourier-transformed EXAFS data |χ(*R*)| (phase-uncorrected) in arbitrary unit (vertical scale) as a function of the interatomic distance (*R*) for $Ru(NH_3)_6Cl_3$ (solid blue) and activated 0.2%Ru–B150 catalyst (solid red) with fitted curves shown by dashed black lines. Contributions of different neighbours for the Ru sites in the activated catalyst are shown by coloured lines with filled area: Ru–X (with neighbouring framework oxygen in red, nitrogen in blue and OH in orange) and Ru–Ru (in violet).

temperature under N_2 (450 °C) resulted in a complete loss of activity. Replacing N_2 with H_2 at 350 °C led to a partial reduction of Ru to the metallic state, as deduced from the formation of 19% hydrogenation products, together with only 42% *tt*-DEM (Supplementary Table 3)[45]. Air activation at 350 °C (leading to potentially volatile Ru oxides) resulted in catalyst deactivation. Thus, metallic Ru(0) (described below) and Ru oxides are not active in this isomerization.

To identify the Ru species formed in the specific pretreatment, in-depth characterization was conducted. Inductively coupled plasma atomic emission spectroscopy (ICP-AES) confirmed the amount of Ru exchanged onto the zeolite to be correct for 0.2%Ru–B150 (±5%). The Ru content was unaltered after activation under N_2 flow at 350 °C, proving that Ru is not volatilized. High-resolution high-angle annular dark-field scanning transmission electron microscopy (STEM-HAADF) imaging was used to examine the activated 0.2%Ru–B150 catalyst. Energy-dispersive X-ray spectroscopy (EDS) was employed to confirm the presence of Ru, as well as Si, Al and O. These results suggest that Ru was homogeneously dispersed throughout the sample (Fig. 3a). High-resolution imaging indicates that the zeolite mostly does not contain metallic particles (Supplementary Fig. 6). However, in a limited number of areas, bright spots were observed. Notably, EDS analysis did not reveal a notable concentration of Ru in these bright spots (Supplementary Fig. 7). The thermal dissociation of NH_3 ligands from $Ru(NH_3)_6^{3+}$ on B150 was followed with both mass spectrometry and FT-IR spectroscopy (Fig. 3b). The dissociation of NH_3 ligands starts at 180 °C, and the NH_3 released up to 350 °C is around 5/6 of the initial amount. At 450 °C, a complete removal of NH_3 takes place, which leads to a concomitant reduction of Ru. Similarly, the decrease in the intensity of N–H stretching bands upon thermal activation was followed with FT-IR spectroscopy (Fig. 3c), with again a decrease of 5/6 at 350 °C. The desorption continues at higher temperatures (Supplementary Fig. 8). Thus, upon activation under N_2 between 200–350 °C, the remaining NH_3 ligands seem to prevent the sintering of Ru and to stabilize it in an atomic form. High-resolution transmission electron microscopy (HR-TEM) and EDS mapping images show the abundance of Ru nanoparticles on the 0.2%Ru–B150 sample activated at 450 °C under N_2, which can be explained by the Ru sintering upon the desorption of the last stabilizing ligands (Supplementary Fig. 9). NH_3 itself (without Ru) was inactive, as confirmed by the absence of isomerization when using NH_3 in solution or an NH_4^+-exchanged zeolite as catalysts (Supplementary Table 3). Similarly, no *tt* was formed when exchanging the zeolite with $RuCl_3$ as the Ru source. On the other hand, the formation of the *tt*-isomer was observed when loading the zeolite with the $Ru(NO)(NO_3^-)_3$ precursor at 0.2 wt% Ru loading (Supplementary Table 3), which indicates that the ligands are not involved in the isomerization mechanism and their role is limited to reducing the Ru mobilization.

X-ray absorption near edge spectroscopy (XANES) and extended X-ray absorption fine structure (EXAFS) data indicate that upon activation under N_2 flow, $Ru(NH_3)_6Cl_3$ loses five of its NH_3 ligands; however, it stays hexa-coordinated by gaining oxygen-containing ligands instead (Fig. 3d,e and Supplementary Table 4). The average oxidation state remains Ru(III) (Supplementary Fig. 10); however, the slight edge shift towards higher energies indicates a lesser ligand-to-metal electron transfer (Fig. 3d). Ab initio simulation of XANES spectra (Fig. 3d) and fitting of the EXAFS data (Fig. 3e) lead us to propose a tentative atomic model of the active sites. The reduced intensity of

the peak in Fourier-transformed EXAFS data, ranging between 2 and 3 Å with respect to the precursor, is explained by the increased local disorder due to different types of neighbouring atoms contributing at 1.89 ± 0.03 Å, which can correspond to H_2O ligands, and at 2.04 ± 0.03 Å and 2.16 ± 0.04 Å, which are hypothesized to be due, respectively, to the remaining NH_3 ligand (detected with temperature-programmed desorption and FT-IR) and bonding with framework oxygens. A small, second-shell peak was modelled by the Ru–Ru contribution (purple) at 2.76 ± 0.02 Å, with an average coordination number of 0.4; it may originate from a small number of Ru clusters. Stabilization of the precursor in the zeolite is crucial for the active-site formation; without this formation, the result is the Ru(0) species (Supplementary Fig. 11f and entry 6 in Supplementary Table 4). In addition, the non-supported $Ru(NH_3)_6Cl_3$ salt was fully reduced after N_2 activation at 350 °C, indicating the necessity of dispersion inside the zeolite to prevent the reduction.

Working towards a process

To bring this catalytic reaction closer to industrial reality, volumetric productivities must be high to convert a concentrated feedstock with fast rates; the catalyst must be stable and the conditions practical. The latter seems fulfilled as ethanol is the solvent of choice and temperatures are moderate (130–175 °C). Ethanol is a sustainable solvent (low cost and readily bio-available) in which DEM is highly soluble and its hydrolysis is avoided[51]. The kinetic study started by determining rates at 150 °C and 175 °C, using a catalyst content of 10 mg ml^{-1} and a *ct*-DEM concentration of 300 mM. Figure 4a shows a faster formation of *tt*-DEM at 175 °C (5.8 $g_{tt\text{-DEM}}\ g_{zeo}^{-1}\ h^{-1}$) in comparison to 150 °C (3.2 $g_{tt\text{-DEM}}\ g_{zeo}^{-1}\ h^{-1}$). However, at both temperatures, the maximal yield of produced *tt*-DEM was similar and limited thermodynamically to around 70%. The reaction order for the isomerization of *ct*-DEM to *tt*-DEM was determined at 150 °C, between 30 and 1,000 mM, using the initial rates method with a power law model. Between 30 mM and 300 mM, rates linearly correlate with reactant concentration, giving an order of 1.05 ± 0.07 (95% confidence interval and a coefficient of determination R^2 = 99.9%), while at higher concentration, the rate still increases, though no longer linearly with the concentration (Supplementary Fig. 12). The positive order allows high volumetric-based and catalyst-weight-based productivities. For a fixed amount of catalyst (50 mg), the data show a linear increase in the productivity reaching a very high value of 160 mM h^{-1} of *tt*-DEM produced at 150 °C (54% conversion) for 300 mM *ct*-DEM (Fig. 4b, dashed line). The productivity increases with a smaller slope to reach 207 mM h^{-1} at 500 mM (53% conversion) and decreases to 176 mM h^{-1} at 1,000 mM (44% conversion). We further modelled the data to include the high concentration regime, and upon fitting the data with various surface reaction models, we found that a substrate-inhibition Langmuir–Hinshelwood model with a single site best reduces the variance, leading to the hypothesis that the surface reaction between a substrate molecule and another substrate adsorbed on an active site deactivates reversibly the latter, causing a drop in the rate above 500 mM substrate concentration (Supplementary Fig. 12b).

At 175 °C, higher productivity values are possible: 368 mM h^{-1} at 500 mM (53% conversion) and 427 mM h^{-1} (that is, 85 g l^{-1} h^{-1}) at 1,000 mM (43% conversion; Fig. 4b, solid line). These reported productivity values compare favourably to literature data for an isomerization process giving *tt*-muconates (Supplementary Table 5). In terms of catalytic productivity, this amounts to 4.1 $g_{tt\text{-DEM}}\ g_{zeo}^{-1}\ h^{-1}$ and 7.3 $g_{tt\text{-DEM}}\ g_{zeo}^{-1}\ h^{-1}$ for a 500 mM solution at 150 °C and 175 °C, respectively. Ultra-concentrated reactions (2.0 M and a 1:1 volume ratio *ct*-DEM/EtOH ≈ 3.2 M) were conducted (Supplementary Fig. 13), and high productivity could still be achieved for the 2.0 M system at 175 °C (434 mM h^{-1} at 43% conversion).

The catalyst is also capable of isomerizing *ct*-MA, in the free acid form, with the isomerization prevailing over the lactonization at low temperature (for example, *tt*-MA/Mlac = 3.6 for 7% *ct*-MA conversion at 100 °C; Supplementary Fig. 14; Mlac, muconolactone). While the lactonization is more difficult to suppress at higher temperature (Supplementary Fig. 15), the tandem esterification–isomerization is a credible alternative to directly convert the acid *ct*-MA to isomerized muconate esters. We succeeded in countering lactonization by performing the esterification on its own or in tandem, with catalytic amounts (3 mM) of homogeneous heteropolyacid $H_4SiW_{12}O_{40}$ (Supplementary Table 6 and Supplementary Fig. 16) and heterogeneous Amberlyst 36 (Supplementary Table 7). In both low and high concentration ranges, the esterification dominates the lactonization, and the produced *ct*-DEM was isomerized in situ to *tt*-DEM with <1% of Mlac (175 °C). The overall productivity values from MA are still important, even if they are lower than the above ester isomerization (64–80 mM h^{-1} for *ct*-MA versus 233–427 mM h^{-1} for *ct*-DEM; Supplementary Table 5). The tandem process thus offers a route to directly couple the highly selective *tt* formation with bio-based *ct*-MA production. The reusability of the esterification catalyst was also tested over consecutive cycles (Supplementary Tables 6 and 7).

The apparent activation energy for the isomerization of *ct*-DEM was calculated from Arrhenius plots between 120 °C and 185 °C based on first-order kinetics of *tt*-DEM formation (Fig. 4c). Operating at a temperature above 160 °C showed an activation energy on the order of 20 ± 7 kJ mol^{-1}, pointing to severe film (external) limitations whereby the diffusion of muconates does not seem capable of following the very high isomerization rates. Similarly, a low activation energy was obtained under a low stirring rate (Supplementary Fig. 17). In the temperature range of 160 °C to 120 °C, the reaction operates under a kinetic regime, with an activation energy of 110 ± 5 kJ mol^{-1}. When studying the isomerization of the bulkier *ct*-DBM ester in the temperature range of 160–130 °C (Fig. 4c, orange plot), an activation energy of 113 kJ mol^{-1} was obtained, which indicates the absence of the pore diffusion limitation. Finally, a new batch of catalyst was tested for the isomerization of *ct*-DEM in an even lower temperature range (80 °C to 120 °C), showing an activation energy of 156 ± 8 kJ mol^{-1}. Combined, these findings point to chemical reaction control of the isomerization between 80 and 160 °C, with perhaps an incline towards diffusion limitations (film limitations, with perhaps pore limitations) at the high end of that range.

The turnover number (TON) was calculated for 0.2%Ru–B150 catalyst with different concentrations of *ct*-DEM (Fig. 4d). Approximately 1,100 mol mol^{-1} was achieved in a solution of 300 mM *ct*-DEM once the system reached its thermodynamic equilibrium. Increasing the concentration of *ct*-DEM (up to 1,000 mM) for the same amount of catalyst showed a higher TON, with a maximal value of 2,800 mol mol^{-1}. The high TON points to an optimal use of the precious metal similar to that of single-atom (or high metal dispersion) catalysis[47,52–54].

The spent catalyst (after 1,000 mM) was characterized to understand deactivation routes and thus possible remediation paths. Thermogravimetric analysis shows 4% formed coke on the spent catalyst, which corresponds to less than 0.7% of the initial amount of *ct*-DEM (300 mM; Supplementary Fig. 18). N_2 physisorption data show a partial loss in the microporous volume on the spent catalyst (dried at 200 °C), mainly related to coke deposition (Supplementary Table 8). ICP-AES measurements confirm a very comparable amount of Ru on the fresh and the spent catalyst (difference of <5%, within the ICP error margin), as well as the absence of any trace Ru in the hot-filtrated liquids. In addition, a hot filtration split test was performed (Supplementary Fig. 19); the recovered liquid was stirred for several hours under the reaction conditions without any further notable conversion in comparison to a blank reaction. High-resolution TEM images and EDS mapping of the spent catalyst show a persisting high dispersion of Ru atoms in the zeolite framework. Some high-contrast particles can be found within the zeolite agglomerates, which can be attributed to Ru by using EDS (Supplementary Fig. 20). However, the small amount of the crystalline Ru particles did not allow their detection with a powder X-ray diffraction technique (Supplementary Fig. 21). The catalyst deactivation is suggested to occur through Ru sintering (Ru nanoparticle formation),

https://doi.org/10.1038/s41929-024-01205-5

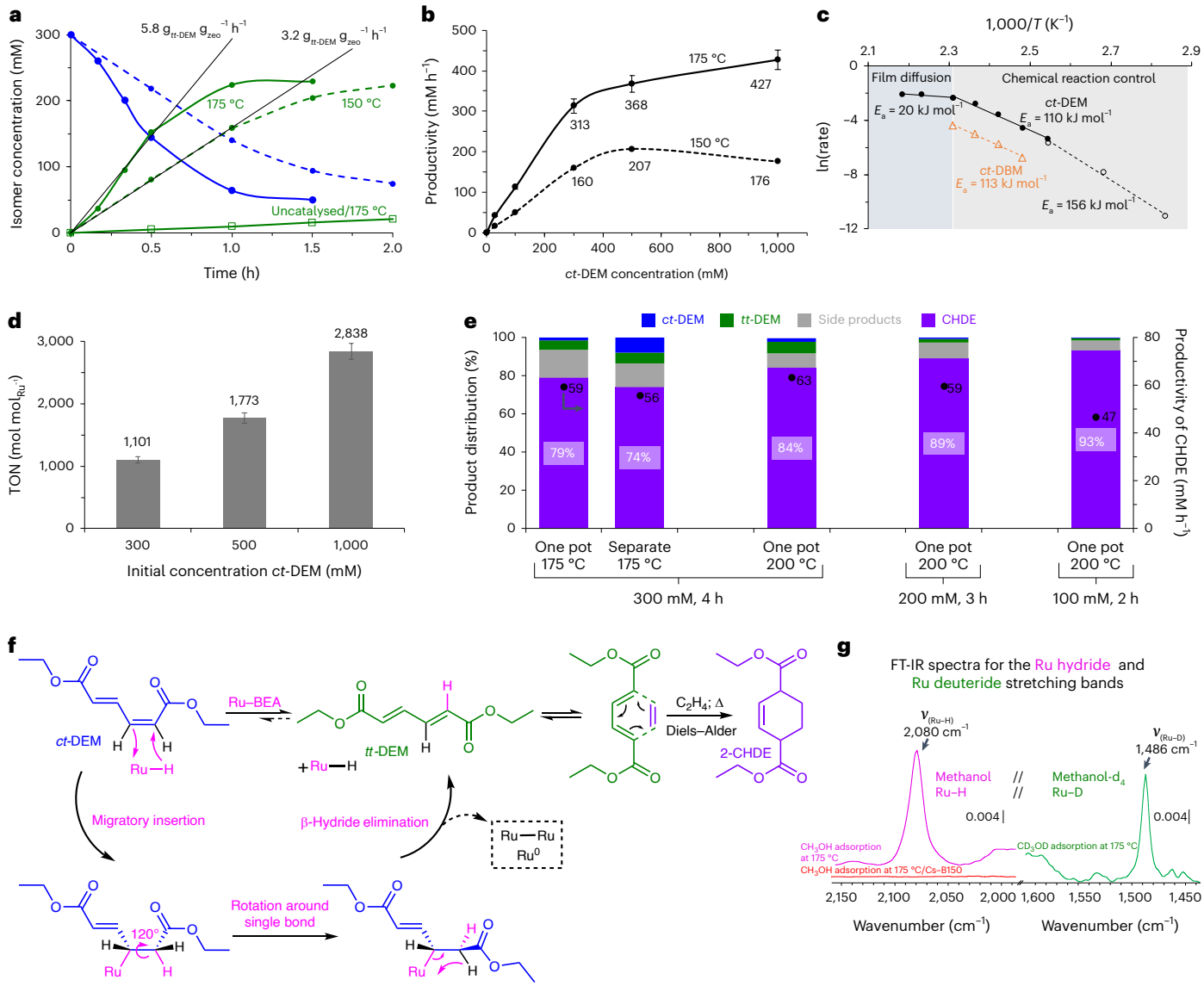

Fig. 4 | Kinetic studies and mechanistic insights of the isomerization of muconates and optimization of the one-pot isomerization and Diels–Alder reactions. a, Kinetic curves of the isomerization of *ct*-DEM (blue) into *tt*-DEM (green) at 150 °C (dashed line) and 175 °C (solid line) for 50 mg 0.2%Ru–B150 catalyst in 5 ml of 300 mM solution. The rate of formation of *tt*-DEM ($g_{tt\text{-DEM}}\ g_{zeo}^{-1}\ h^{-1}$) was estimated from the slopes (black lines) using the reaction values in the ranges of 0 to 0.5 h for the reaction at 175 °C and 0 to 1 h for the reaction at 150 °C. **b**, Productivity values of the isomerization process at 150 °C and 175 °C (50 mg, 5 ml) as a function of the initial concentration of *ct*-DEM. The error bars correspond to the percentage of variation (around 4.5%) obtained from three repetitive reactions at identical conditions. **c**, Arrhenius plot of the isomerization of 300 mM *ct*-DEM in ethanol in a temperature (*T*) range from 80 °C to 185 °C with the type of regime labelled on top (values based on the conversion of *ct*-DEM). The rate was estimated in mM h^{-1}. A different synthesis batch of the same catalyst was used for experiments in the 80–120 °C zone. **d**, TON per Ru values were calculated in the equilibrium isomerization zone for different concentrations of *ct*-DEM. The error bars correspond to the percentage of variation (around 4.5%) obtained after calculating the standard deviation from three repetitive reactions at identical conditions. **e**, The product distribution for several Diels–Alder reactions (in separate or a one-pot isomerization/Diels–Alder process). These reactions were performed at the indicated concentrations, temperatures and times in the presence of 40 bar ethylene (loaded at room temperature) with 6 mg ml^{-1} of zeolite. Side product nomination accounts for hydrogenation products (mono- and di-hydrogenated), oligomers and the loss in the carbon balance. A 50 ml reaction was also performed (Supplementary Fig. 28). **f**, Reaction scheme for the one-pot isomerization/Diels–Alder process showing the proposed mechanism for the Ru-catalysed isomerization. After isomerization, the *tt*-DEM can undergo Diels–Alder cycloaddition in the role of diene due to its specific geometry. The reaction was also proven to work with methyl and butyl muconic esters. **g**, The FT-IR spectra of the formation of Ru hydride and Ru deuteride peaks followed by the adsorption of methanol and methanol-d_4, respectively, over pre-activated 0.2%Ru–B150 zeolite and Cs–B150 zeolite.

possibly after the loss of all ligands, as a strong ligand is expected to somewhat protect the Ru from agglomerating.

Catalyst regeneration (after 1,000 mM) was attempted using several methods (labelled 'Reg 1' to 'Reg 3' in Supplementary Fig. 22; details in Supplementary Note 1); however, only a mediocre regeneration ability was achieved, reaching at best 53% of the initial activity with a cumulative TON of 4,100 mol mol^{-1} (Supplementary Fig. 23). EXAFS data on the spent sample shows that the deactivation of the catalyst is associated with the formation of Ru(0) and Ru(II) (vide supra) and the formation of Ru–Ru bonds (Supplementary Fig. 11d and entry 4 in Supplementary Table 4). These species seem to revert partially (Ru(0)) or fully (Ru(II)) to Ru(III) during reactivation (Reg 2), as observed from a linear combination fit on the experimental samples using reference XANES spectra (Supplementary Fig. 11). The recovery

of the oxidation state of Ru does not necessarily imply the regeneration of the initial Ru species, since the isomerization activity was not fully recovered with this method. Moreover, the possible redispersion of Ru nanoparticles did not improve the regeneration ability. A preliminary techno-economic analysis was performed, showing the potential industrial relevance of this technology, where the metal recovery from the catalyst (post-reaction) can effectively reduce the cost of the use of Ru, as detailed in Supplementary Note 4 and Supplementary Table 12.

Mechanistic considerations with Ru hydride species

A plausible mechanism of the isomerization is illustrated in Fig. 4f, in which a Ru hydride complex catalyses the isomerization[46,55]. After the generation of the Ru–H (or Ru–D) complex, the hydride insertion occurs on the C=C double bond of muconates; furthermore, a rotation of the single bond takes place, which is followed by a β-hydride elimination to regenerate the metal–hydride complex while producing the muconates in the desired configuration. The alcohol solvent plays the role of activator (co-reagent) since a hydride donor is required to produce the metal–H species[56]. To confirm this, different solvents were tested, and an absence of isomerization was observed when using ethyl acetate, acetone and toluene; however, the isomerization was successful in methanol, ethanol and butanol with their respective muconic esters. Also, the formation of hydrogenation products (as side products) suggests that a Ru hydride is operating. The rate of formation of *tt*-DEM was followed in three different alcohols with different H-donor capacities, namely, isopropanol > methanol > ethanol (Supplementary Fig. 24). The results show the highest production rate of *tt*-DEM when using isopropanol (the alcohol with the highest H-donor capacity); however, the very small variation in *tt*-DEM yield is insufficient to define the hydride generation as the rate-determining step of the two reactions. For a better comparison, we studied the isomerization rate when using methanol and deuterated methanol (methanol-d_4) where the results show that the use of methanol-d_4 slows the reaction rate by a factor of around 1.46, which highlights the presence of a kinetic isotopic effect (Supplementary Fig. 24a,d). Given the similar rates with differently acidic alcohols, one could suspect the migratory insertion to be rate limiting (slower in a Ru deuteride). A further proof is the identification of 1,1-diethoxyethane in the reaction products (Supplementary Fig. 25), which results from the reaction of acetaldehyde with ethanol[57]. For an even better proof of the mechanism, we studied the isomerization products of *ct*-DMM in deuterated methanol (methanol-d_4) by ^{13}C NMR (Supplementary Fig. 26). In the proposed mechanism, methanol-d_4 acts as a D source to generate the Ru–D species (or Ru–H from methanol), which transfers the deuterium to the produced *tt*-DMM, with the formation of a C–D bond. From ^{13}C NMR data (Supplementary Fig. 26), the presence of C–D coupling on the *tt*-DMM was noticed after isomerization, giving a solid confirmation of the proposed mechanism. In addition, these findings point out that the deuteride insertion occurs selectively, whereby the D is incorporated at the C-2 while the Ru bond is formed with C-3, probably due to electronic or steric effects[58]. As a thermodynamic equilibrium exists between *ct*-DMM and *tt*-DMM, an isotopic scrambling was expected at prolonged reaction time, which was confirmed by ^{13}C NMR data showing the presence of a C–D coupling on both the C-2 and C-5 atoms of *ct*-DMM, but not on C-3 and C-4 (Supplementary Fig. 26). The generation of the Ru–H bond was confirmed with FT-IR measurements following the adsorption of methanol vapour on the Ru–B150 zeolite at 175 °C (Fig. 4g). After loading gas-phase methanol, a peak at 2,075–2,080 cm^{-1} was observed on the Ru–zeolite, which is assigned to the stretching vibrations of Ru–H (refs. 59–61). However, the formed Ru–H species on the zeolite were unstable in the absence of methanol or under desorption conditions (Supplementary Fig. 27 and Supplementary Note 2). Importantly, the adsorption of methanol-d_4 was also performed, and a new peak, centred at around 1,486 cm^{-1}, was observed, which is in line with the expected position of the isotopic shift in FT-IR spectroscopy (Fig. 4g, Supplementary Fig. 27 and detailed calculation in Supplementary Note 2). These experiments are direct proof of the Ru hydride mechanism and show a spectroscopic signature of an atomically dispersed Ru hydride complex in zeolite. Finally, to show the great potential of the Ru-based catalyst we have developed, we showed its successful use in wider applications, such as hydride transfer reactions, as shown in Supplementary Table 9.

Coupled isomerization and Diels–Alder reactions

The distribution of around 70:30 *tt*-DEM/*ct*-DEM is a thermodynamic barrier. Yet, this barrier requires a cumbersome isomer separation, which can be performed through a back-hydrolysis under basic conditions (>2 equiv. NaOH) of DEM into MA. One of the reactions that most benefits from a *trans*,*trans* configuration is the Diels–Alder cycloaddition, as the rearrangement of the double bonds in the *tt*-isomer allows the atom-efficient coupling of *tt*-muconates and a dienophile (Fig. 4f)[21,62]. Hence we looked into coupling the isomerization reaction directly with this *tt*-DEM-consuming reaction to drive the reaction to higher *ct*-DEM conversion. So, in a one-pot reaction under ethylene pressure, *ct*-DEM was transformed into CHDE through a non-catalysed Diels–Alder cycloaddition of ethylene to *tt*-DEM (Fig. 4e,f). A 50 ml solution of 300 mM *ct*-DEM in ethanol was mixed with 300 mg 0.2%Ru–B150 (6 mg ml^{-1}) in a Parr reactor loaded at 25 °C with 40 bar ethylene. Supplementary Fig. 28 shows the product distribution of the coupled isomerization/Diels–Alder reactions at 175 °C. The thermodynamic equilibrium between the muconates was rapidly attained within 1 h, with the non-catalysed Diels–Alder reaction being the rate-determining step. Some 19% CHDE was formed after 1 h, and the amount kept increasing with time, clearly consuming *tt*-DEM, boosting its production from *ct*-DEM and pushing the *ct*-DEM to near full conversion (versus the 70% typically observed in the absence of ethylene). After 4 h of reaction, 97% of the *ct*-DEM was converted into 79% CHDE yield (81% selectivity) with 7% of *tt*-DEM remaining at a productivity of 59 mM h^{-1}. The side products consist of identified muconic oligomers (the main products identified) and hydrogenation products, and non-identified/non-recovered products. The formation of side products was found to be favoured by the high concentration of *tt*-DEM present in the first hour of the reaction. Besides optimizing ethylene pressure (0 to 40 bar) and solvent (Supplementary Table 10, Supplementary Note 3 and Supplementary Figs. 29–31), we analysed the separation of the isomerization and Diels–Alder reactions, with a filtration step in between during which ethylene is added. The results indeed show a decrease in side product formation but only 74% CHDE (versus 79% in the coupled process). This is easily explained by the lack of further isomerization of the remaining *ct*-DEM (Fig. 4e). To reduce the residence time of *tt*-DEM in the one-pot process, we favoured the Diels–Alder cycloaddition by increasing the reaction temperature to 200 °C. At the same time we can benefit from the film diffusion limitations above 175 °C (Fig. 4c) as the rate of *tt*-DEM formation will not increase a lot. As shown in Fig. 4e, the CHDE yield increased to 84% at 200 °C, together with a reduction in side products (Fig. 4e). A final optimization, away from side products, is achieved by reducing the substrate concentration (200 mM and 100 mM lead to 89% and 93% CHDE, respectively; Fig. 4e). While this curtails the productivity of the process (59 mM h^{-1} at 300 mM to 47 mM h^{-1}), highly concentrated solutions on the other side of the spectrum (Supplementary Figs. 32 and 33) suffer modest yields. In line with the literature, the dehydrogenation of CHDE (from the 300 mM one-pot solution) to diethyl terephthalate was easily proven using a Pd/C catalyst (Supplementary Table 11)[32].

Conclusions

This work presents a strategy to design atomically supported ionic Ru on beta zeolite catalysts and use them in a heterogeneously catalysed pathway to obtain *tt*-muconates from *ct*-muconates. The unique activity of our Ru-based catalysts led to high productivity of *tt*-muconates (427 mM h^{-1}) and a selectivity above 95%. The catalysis features very high turnovers per Ru of around 2,800 mol mol^{-1} (and 4,100 mol mol^{-1} after

regeneration), arguably due to the high dispersion of ionic Ru active sites in the channels of the support zeolite. The isomerization of the bio-based MA itself was also demonstrated to produce the *tt*-isomer in a selective coupled esterification–isomerization process. The equilibrium of the isomerization was pushed towards *tt*-muconates when the isomerization was coupled to a Diels–Alder reaction in one pot. As a result, the formation of CHDE (terephthalic intermediate) could be demonstrated directly from *ct*-muconates. The isomerization mechanism occurs via Ru hydride intermediates generated from the alcohol solvent, as was evidenced by isotopic-labelled NMR and FT-IR measurements.

The developed isomerization process pushes the feasibility of the large-scale production of *tt*-muconates: little waste is produced (<10 mol%) and a high TON is attained (2,800 mol mol^{-1} in one reaction cycle), in addition to good volumetric and catalytic productivity (427 mM h^{-1}, which corresponds to 60.6 g of MA equivalent per litre of solution per hour). The latter two results combine into low catalyst consumption (100 μg_{Ru} per gram *ct*-DEM in 1.0 M reactions)[2,63]. A preliminary techno-economic analysis was performed showing the potential industrial relevance of this technology. In addition, the productivity shown for this isomerization process is higher than that reported for the biotechnological production of MA (17 mM h^{-1} or 2.5 g l^{-1} h^{-1}). Enabling the application of bio-based MA will depend on advances in its production (rates and cost); a bridge between the actual bio-based production of MA and the isomerization can now be established. Research could target promising solvents to extract MA from the fermentation broth that also allow the direct follow-up by the (here proven) tandem esterification and isomerization. Isolating *tt*-muconates could be a hurdle to the process, but a back-hydrolysis into the non-soluble *tt*-MA could be performed to isolate the latter from the other isomers. For dimethyl muconate, the low solubility of the *tt* form in methanol indeed led to an easy recovery after its partial precipitation (with around 60–80% recovery). Otherwise, coupling isomerization with another chemical transformation was shown to help in pulling the reaction equilibrium to full conversion of the *ct*-isomer (as well as the *tt*-isomer). Combining isomerization with Diels–Alder and dehydrogenation reactions opens up a direct route to produce terephthalates from bio-based *cc*-muconates. Beyond the isomerization of muconates, the developed strategy offers access to highly active heterogeneous Ru hydride catalysis in a zeolite. This catalyst in itself, but also the strategy to design and activate such catalysts, offers opportunities to develop second-generation Ru-on-zeolite catalysts for hydride-catalysed reactions and Ru chemistries (for example, hydride transfer hydrogenation). In addition, dedicated zeolite syntheses could expand these possibilities by targeting specific hosting arrangements for Ru siting.

Methods

Materials

The zeolites ZSM-5 140 (CBV28014), Beta 12.5 (CP814E) and Beta 150 (CP811C-300) were supplied from Zeolyst. USY250 (HSZ-300 390HUA) and Beta 250 (HSZ-900 980HOA) were supplied by Tosoh. Beta 75 (CZB150) was provided by Clariant. The *cc*-MA was purchased from Fluorochem with a purity of >99%. Ethanol (99.8%), *n*-butanol (99%), *n*-heptane (>99%) and anhydrous magnesium sulfate, $MgSO_4$ were supplied by Fisher. Ethyl acetate (99.5%); dichloromethane (99%); methanol (99%); 96% sulfuric acid in water, H_2SO_4/H_2O; and hexaminеruthenium(III) chloride, $Ru(NH_3)_6Cl_3$ (98%) were supplied by Acros. Sodium chloride (>99.5%) was supplied by Carl Roth, and caesium acetate, CH_3COOCs (98%) was supplied by Alfa Aesar. The 28–30% ammonia solution in water was supplied by Merck. The pressurized ethylene (C_2H_4) bottle (>99.95%, 70 bar) was supplied by Air Liquide.

Preparation of muconic and muconate isomers

The *ct*-MA was formed by the isomerization of 2.0 g *cc*-MA in 100 ml deionized water at 80 °C for 75 min. After the reaction, the solution was cooled (overnight) to room temperature, and crystals of pure *ct*-MA started to form. After filtration on a paper filter and being dried at 60 °C under air, around 1.3–1.4 g of isolated *ct*-MA were recovered. Furthermore, water was removed using a rotary evaporator, and the remaining substrate containing Mlac and *ct*-MA was washed with dichloromethane. The remaining solid substrate was filtrated and dried under air at 60 °C, and an additional 0.4–0.5 g of pure *ct*-MA was collected; the total yield was between 85–95% (ref. 20).

The esterification of *ct*-MA into *ct*-DEM was performed by adding 2.0 g *ct*-MA and a few drops of H_2SO_4/H_2O in 100 ml ethanol. After a 24 h reflux (temperature of oil bath, 85 °C), ethanol was removed under reduced pressure and the remaining liquid was extracted with ethyl acetate. The organic phase was dried over $MgSO_4$ and the solvent was removed under reduced pressure to obtain pure *ct*-DEM with 90–95% yield. Similarly, methanol and *n*-butanol were used to obtain *ct*-DMM and *ct*-DBM, respectively. The *tt*-muconates (*tt*-DMM, *tt*-DEM and *tt*-DBM) were prepared using the same procedure as *tt*-MA.

Preparation of the Ru–zeolite catalysts

Prior to ruthenium loading, the zeolite powder was exchanged with NH_4^+, Na^+ and Cs^+. The NH_4^+ exchange was performed in an aqueous solution of ammonia (0.015 M) at room temperature for 16 h (200 $ml_{solution}\ g_{zeolite}^{-1}$). The Na^+ form was obtained from the NH_4^+ zeolite via two successive ion-exchange steps at room temperature lasting 16 h each, using 100 ml of 1.0 M aqueous solution of NaCl per 1 g of dry zeolite. Furthermore, the Cs^+ form was obtained after two successive room temperature ion-exchange steps (48 h and 72 h) with a 0.1 M aqueous solution of caesium acetate (25 ml g^{-1}). For each exchange step, the zeolite powder was recuperated via centrifugation, washed with water and air dried at 80 °C (ref. 45).

Finally, the zeolites were loaded with 0.2 wt% Ru by ion exchange after adding 1 g of the Cs–zeolite to 100 ml aqueous solution containing the required amount of ruthenium precursor, $Ru(NH_3)_6Cl_3$. After 24 h, the zeolite powder was filtered, washed once with distilled water and dried at 50 °C.

Isomerization reactions

Prior to activation, the zeolite powder was self-pressed, crushed and sieved to obtain granules between 250 µm and 500 µm. The activation conditions were found to influence the activity of the catalyst in the isomerization reactions; thus, different activation conditions were applied: no activation, 120 °C for 2 h under N_2 flow (100 ml min^{-1}), 350 °C for 2 h under N_2 flow (100 ml min^{-1}), 350 °C for 2 h under H_2 flow (100 ml min^{-1}), 350 °C for 2 h under static air and 450 °C for 2 h under N_2 flow (100 ml min^{-1}). A heating rate of 2 °C min^{-1} was used from room temperature to 200 °C followed by an isotherm for 0.5 h. Further heating at 3 °C min^{-1} was performed from 200 °C to 350 °C and followed by a final isotherm for 2 h.

The formation of *tt*-isomer from the *ct* form was performed in a 12 ml pressure reactor (Supplementary Fig. 34). Solutions of 5 ml alcohol (methanol, ethanol or butanol) or other solvents containing 30 mM to 3,200 mM *ct*-muconates (*ct*-MA, *ct*-DMM, *ct*-DEM or *ct*-DBM) were mixed with 50 mg of catalysts. The reactor was flushed with N_2 before being sealed at 14 bar N_2 at 25 °C. Reactions were performed at various temperatures ranging from 80 °C to 185 °C, and the conversion was followed by a timed sampling. The product distribution was determined by gas-phase chromatography following the analysis described below.

The tandem esterification–isomerization reaction was performed in the 12 ml pressure reactors where a solution of 5 ml ethanol containing 100–1000 mM *ct*-MA was mixed with 3 mM silicotungstic acid ($H_4(SiW_{12}O_{40})$) and 30 mg of 0.2%Ru–B150, respectively, as the esterification and isomerization catalysts. The reactor was flushed and sealed with N_2 (14 bar at 25 °C). Reactions were performed at 150 °C or 175 °C, and the conversion and product distribution were determined by gas chromatography and ^{1}H NMR, following the procedures described

below. The yields of *ct*-DEM and *tt*-DEM were calculated using gas chromatography analysis. The ^{1}H NMR was used to confirm the absence of the carboxylic acid signals after the reaction and to calculate the Mlac yield (peak at 7.80 ppm in DMSO-d_6 and using $DMSO_2$ as external standard). The integration of the respective peaks of the ethyl groups was in good agreement with the values corresponding to a complete di-esterification (and not only a mono-esterification). The ratio of the area of CH_2–O peak on the area of C–H peak of muconate $A_{(CH2-O\,peak)}/A_{(C-H\,muconate)}$ was around 4.1 (the expected value for complete di-esterification is 4.0). After the reaction, the zeolite was recovered by centrifugation. The homogeneous silicotungstic acid was extracted with liquid–liquid extraction (ethyl acetate/water), and later the water was removed under reduced pressure (or dried under N_2 flow). The recovered amount (assumed to be pure silicotungstic acid) was around 80–90% and was used in further catalytic cycles.

For the ease of separation and recovery, Amberlyst 36 (Aldrich) was used as a heterogeneous catalyst for the esterification in the tandem process. The reactions were performed at 150 °C under the same reaction conditions in the presence of 250 mg of Amberlyst 36 and 30 mg of 0.2%Ru–B150 catalyst in 3 ml ethanol.

Tandem isomerization and Diels–Alder reaction

The one-pot (tandem) isomerization of *ct*-muconates to *tt*-muconates and the Diels–Alder cycloaddition of ethylene (C_2H_4) with *tt*-muconates was performed in a pressure reactor at temperatures ranging between 150 °C and 200 °C. Herein, a solution of 3 ml to 50 ml of alcohol containing 300–2,000 mM *ct*-muconate was mixed with 0.2%Ru–Beta 150 (6 mg ml^{-1}) catalyst under an initial pressure ranging from 14 bar to 40 bar C_2H_4 (sealed at 25 °C). The reactor was sealed, and the pressure increased by heating, for example, up to 80 bar when the reactor reached 175 °C (starting from 40 bar). The conversion was followed with a timed sampling, and the product distribution was determined by gas chromatography (more below).

ICP-AES

The elemental analysis was performed using an ICP-AES instrument (PerkinElmer Optima 3300 DV) with signals for Ru, Al and Si at 267.9, 308.2 and 251.6 nm, respectively. Prior to ICP-AES measurements, 50 mg of the zeolite sample was dissolved in 0.5 ml hydrofluoric acid and 1 ml aqua regia. After a few hours, the solution was neutralized with 15 ml boric acid solution (0.49 M) and further diluted to 100 ml in deionized water. A sample was taken of the solution and diluted 25 times in 0.42 M aqueous nitric acid (HNO_3) solution[64]. A calibration curve for Ru standards was plotted using five solutions with the following concentrations: 0.01, 0.02, 0.03, 0.04 and 0.05 ppm.

FT-IR spectroscopy

The densities of Brønsted and Lewis acid sites were determined using pyridine adsorption followed by FT-IR spectroscopy on a Nicolet 6700 spectrometer equipped with a deuterated triglycine sulfate detector[65]. Prior to analysis, samples were self-pressed into precisely weighed wafers of a density of around 10 mg per cm^2. The wafers were degassed in situ (<0.1 mbar) at 400 °C (5 °C min^{-1}) for 6 h. After degassing, a reference spectrum of the activated material was recorded at 150 °C with an accumulation of 64 scans at a resolution of 4 cm^{-1} (ref. 42). After further cooling to 50 °C, pyridine vapour was introduced on the samples until saturation, followed by a thermal desorption at 150 °C under vacuum (<0.1 mbar) for 1 h to remove weakly adsorbed species. A spectrum was recorded at the end of this step and compared to the reference spectrum. The densities of Brønsted and Lewis acid sites were determined by integrating the area of their characteristic bands ('v8a' at ~1,545 cm^{-1} for pyridinium ions (PyH^+) and 'v19b' at ~1,445 cm^{-1} for coordinated pyridine (PyL)) and using their relative molar absorption coefficients: $\varepsilon(PyH^+)$ = 1.67 cm µmol^{-1} and $\varepsilon(PyL)$ = 2.22 cm µmol^{-1} (refs. 66,67).

The thermal desorption of NH_3 ligands was performed on the same set-up; however, the vacuum was replaced with a N_2 flow of 50 ml min^{-1}. The desorption was followed from 180 °C to 400 °C with a heat ramp of 5 °C min^{-1} and an isotherm of 20 min at 350 °C and 400 °C.

The adsorption of methanol was performed over Ru–beta zeolite. After preparing the zeolite wafer and activating it under N_2 flow (100 ml min^{-1}) at 300 °C, the temperature was reduced to 175 °C, and the N_2 environment was replaced by a vacuum of around 5×10^{-2} mbar. Methanol vapour (15–20 mbar) was introduced into the cell over several doses, and spectra were collected (64 scans with 2 cm^{-1} resolution) until the surface was saturated. Directly, after cutting the methanol flow, spectra were acquired to follow the evolution of the remaining methanol species on the surface (measured at 150 °C and 200 °C).

N_2 physisorption

N_2 adsorption isotherms in the relative pressure (P/P_0, absolute/saturation pressure) range of 0.001 to 0.99 bar were measured on a Tristar II 3020 instrument. The samples were dried at 300 °C for 6 h prior to analysis. The linearity of fitting for the Brunauer-Emmett-Teller (BET) specific surface area was 0.9999. The total pore volume was calculated by the Gurvich rule at a P/P_0 = 0.95, while the micropore volume was deduced using the *t*-plot (statistical thickness) method[44].

STEM and EDS

HAADF-STEM and EDS were performed on an aberration-corrected cubed Thermo Fisher Advan-TEM Titan microscope equipped with a Super-X EDS detector operating at 300 kV. Also, an aberration-corrected JEOL ARM200F microscope operating at an acceleration voltage of 200 kV and equipped with a Centurio EDS detector was used. EDS analyses were performed by acquiring at least 150 frames at a higher dosage of 2×10^4 e^- A^{-2} (e^-, electron) to ensure enough counts. The samples were prepared via drop-casting a sonicated particle suspension on a holey carbon-coated Cu TEM grid (Cu, 400 mesh, Agar Scientific).

EXAFS and XANES

X-ray absorption spectroscopy data were collected at the BM23 beamline of the European Synchrotron Radiation Facility (ESRF; Grenoble, France). All samples were pressed into pellets of optimal thickness and measured in transmission mode. The photon intensity before and after passing through the sample was registered by ionization chambers. A Si(311) monochromator was operated in continuous scanning mode. For better statistics, multiple scans were collected and averaged, with a total acquisition time of 10–20 min per sample. Ru foil was measured simultaneously with the samples, using a third ionization chamber for energy calibration. Spectra processing and EXAFS fitting were performed in the Demeter package[68]. Theoretical XANES spectra were calculated within a finite difference method of the FDMNES code for three-dimensional atomic models pre-optimized at the DFT level of theory[69], and the convolution parameters were optimized by PyFitIt code[70].

Thermogravimetric analysis

Thermogravimetric analysis was performed on a Q500 instrument (TA Instruments) while heating the sample from 25 °C to 700 °C (5 °C min^{-1}) under a flow of 90 ml min^{-1} of O_2.

Temperature-programmed desorption with He flow

Temperature-programmed desorption of NH_3 ligands under a He flow was measured on a 250 mg sample, loaded in a quartz reactor tube (5 mm inner diameter) packed with quartz wool and placed in a heating furnace. The thermal activation followed a ramp of 5 °C min^{-1} from room temperature to 350 °C for 1 h, then to 450 °C where it was held for 1 h under a flow of 20 ml min^{-1} of He. A quadrupole mass spectrometer (Pfeiffer Omnistar Quadstar 422) equipped with a scanning electron microscopy detector measured the current intensities for ions with the following masses: 2, 4, 16, 17, 18, 28 and 35 AMU. Software (Quadstar 422)

converted the intensities to molar fractions after calibration. We calibrated for H_2, He, NH_3, H_2O and N_2 gases. Since we analysed gases under dilute conditions, we approximated the molar flow-rate for each species as the product of the inlet flow-rate with the molar fraction measured at the outlet of the reactor. Area integration after baseline subtraction of the molar flow-rate over the time on stream gives the molar amount of gas desorbed/reacted over the sample.

Powder X-ray diffraction

The structure and crystallinity of samples were investigated using powder X-ray diffraction on a high-throughput STOE STADI P Combi diffractometer in transmission mode, with focusing Ge(111) monochromatic X-ray inlet beams and with Cu Kα radiation (wavelength, $\lambda = 1.5406$ Å), operated at 20 kV. A scanning time of 10 min was used for the analysis of each sample for a range from $2\theta = 0$ to 60°, where 2θ is the angle between the transmitted beam and reflected beam.

Thermodynamic equilibrium calculations

The Aspen HYSYS chemical process simulator lacks the thermodynamic properties of *ct*-MA and *tt*-MA and the corresponding esters, but *ct*-hexa-2,4-diene and *tt*-hexa-2,4-diene are present. The *ct*-hexa-2,4-diene and *tt*-hexa-2,4-diene have the same structure as the muconic esters, except for the terminal functionalities, and are good template molecules to simulate the thermodynamic equilibrium calculations to further validate our equilibrium assumptions. Aspen HYSYS calculates the composition of a system composed of *ct*-hexa-2,4-diene isomerizing to *tt*-hexa-2,4-diene (solvent-less), using a Gibbs reactor and UNIQUAC fluid package. The influence of pressure is null but maintains the mixture in liquid phase at 20 bar, and a sensitivity analysis probes the effect of temperature on the thermodynamic equilibrium (Supplementary Fig. 3). We regressed the kinetic data for the catalytic isomerization of *ct*-DEM with the least square function to find the best-fitting model based on Pearson's product moment. We derived the proposed model (Langmuir–Hinshelwood forward surface reaction model with substrate inhibition, where [S] is the concentration of S, the catalyst's vacant sites) assuming all elementary surface reaction steps are in equilibrium except the surface reaction, which is rate limiting and is assumed to be forward only. The inhibition elementary step is calculated from the surface reaction with substrate (*ct*-DEM) with an already occupied site (*ct*-DEM-S):

$$\text{Adsorption} : [ct\text{-DEM}] + [\text{S}] \leftrightarrow [ct\text{-DEM-S}] \quad (1)$$

$$\text{Reaction} : [ct\text{-DEM-S}] \rightarrow [tt\text{-DEM-S}] \quad (2)$$

$$\text{Desorption} : [tt\text{-DEM} - \text{S}] \leftrightarrow [tt\text{-DEM}] + [\text{S}] \quad (3)$$

$$\text{Inhibition substrate on adsorbed substrate} : [ct\text{-DEM}] + [ct\text{-DEM} - \text{S}] \leftrightarrow [ct\text{-DEM} - ct\text{-DEM} - \text{S}](\text{Inactive}) \quad (4)$$

Permutation of the other three, different inhibitions gave lower scores; these were inhibition substrate on adsorbed product, inhibition product on adsorbed substrate and inhibition product on adsorbed product.

Combining the four elementary steps with the assumption that the reaction is rate determining and the balance of the total number of active sites give the following rate expression for turnover frequency (TOF):

$$\text{TOF}\ (\text{mol}\text{mol}_{\text{Ru}}^{-1}\text{h}^{-1}) = \frac{k_s K_a [ct\text{–DEM}]}{1 + [ct\text{–DEM}] K_a + [tt\text{–DEM}]/K_d + [ct\text{–DEM}]^2 K_a K_i} \quad (5)$$

where the items in brackets are the molar concentrations of substrate or product (mol l^{-1}); [*ct*-DEM] corresponds to the remaining concentration of *ct*-DEM after isomerization; and K_a, K_d and K_i are the respective equilibrium constants for adsorption, desorption and inhibition elementary steps and are regressed with k_s, the surface reaction forward kinetic, to fit the turnover frequency of the isomerization reaction at 1 h (Supplementary Fig. 12). The estimated regressed coefficients are $k_s = 1.6 \times 10^6$ h^{-1}, $K_a = 3.6 \times 10^{-3}$ m^3 mol^{-1}, $K_d = 1.3 \times 10^5$ mol m^{-3} and $K_i = 1.8 \times 10^3$ m^3 mol^{-1}.

Gas-phase chromatography

The product distribution of both isomerization and Diels–Alder reactions was calculated using an Agilent Technologies 6890N gas chromatography instrument equipped with a DB-17 capillary column of 0.32 mm internal diameter and N_2 as a gas carrier. Some 0.2 µl of the solution was injected at 250 °C with a split ratio of 25:1 and driven to the column (initially at 80 °C) at a flow-rate of 2.6 ml min^{-1}. After 5 min at 80 °C, the temperature was increased to 200 °C (10 °C min^{-1}) and held for 3 min, and then increased to 280 °C (20 °C min^{-1}) and held for 6 min. The flame ionization detector was maintained at 320 °C. Some *n*-heptane was used as an internal standard, and calibration curves were performed for the following components: *ct*-DMM ($A_{ct\text{-DMM}}/A_{\text{heptane}} = 1.144 \times$ [*ct*-DMM]/[heptane]), *ct*-DEM ($A_{ct\text{-DEM}}/A_{\text{heptane}} = 1.408 \times$ [*ct*-DEM]/[heptane]) and *ct*-DBM ($A_{ct\text{-DBM}}/A_{\text{heptane}} = 1.928 \times$ [*ct*-DBM]/[heptane]), and similar response factors were used to the respective *tt*-isomers after confirming the similarity between the response factors of *ct*-DEM and *tt*-DEM. The calibration curve of the Diels–Alder product versus *n*-heptane (CHDE) was performed after its preparation (from *ct*-DEM), purification (column chromatography on silica gel using pentane/ethyl acetate, 9:1 as eluant) and isolation (solvent removal under reduced pressure). A correction to the number of carbons of cyclohexene-1,4-dicarboxylic acid dimethyl ester (CHDM) and cyclohexene-1,4-dicarboxylic acid dibutyl ester (CHDB) (versus CHDE) was performed.

A few experiments (during the first screenings; Supplementary Table 10) were performed without the use of an internal standard. The product distribution was estimated by correcting the integrated area of each compound to their relative carbon numbers. The same carbon number was counted for the respective hydrogenation products and muconic oligomers.

All the reaction products were identified based on retention times, using pure components or mixtures with various ratios as references (examples of chromatograms are given in Supplementary Figs. 35 and 36):

- The *n*-heptane (~1.5 min)
- The *tt*-muconates: *tt*-DMM (~13.3 min), *tt*-DEM (~15.0 min), *tt*-DBM (~20.1 min)
- The *ct*-muconates: *ct*-DMM (~13.8 min), *ct*-DEM (~15.3 min), *ct*-DBM (~20.3 min)
- The Diels–Alder products: CHDM (~15.9 min), CHDE (~17.0 min), CHDB (~21.9 min)

In addition, side products were identified as being mainly hydrogenation products: dimethyl adipate (~14.3 min), dimethyl hexenedioate (~12.5 min), diethyl hexenedioate (~14.9 min) and diethyl hexenedioate (~19.5 min), in addition to muconic oligomers (~22.5–26.5 min).

^{1}H and ^{13}C NMR

The spectra were recorded on Bruker Advance 300, 400 and 600 MHz spectrometers with a BBI 5 mm probe using DMSO-d_6 solvent (Sigma-Aldrich) and $DMSO_2$ as the standard. The ^{1}H NMR spectra and the corresponding chemical shifts of different products are given in the Supplementary Information, pages 32–35.

Data availability

The data that support the findings of this study are available in the main text and the Supplementary Information file or from the

corresponding author upon reasonable request. Source data are provided with this paper.

References

1. Vercammen, J. et al. Shape-selective C–H activation of aromatics to biarylic compounds using molecular palladium in zeolites. *Nat. Catal.* **3**, 1002–1009 (2020).
2. Lange, J.-P. Performance metrics for sustainable catalysis in industry. *Nat. Catal.* **4**, 186–192 (2021).
3. Brandi, F., Khalil, I., Antonietti, M. & Al-Naji, M. Continuous-flow production of isosorbide from aqueous-cellulosic derivable feed over sustainable heterogeneous catalysts. *ACS Sustain. Chem. Eng.* **9**, 927–935 (2021).
4. Dusselier, M., Van Wouwe, P., Dewaele, A., Makshina, E. & Sels, B. F. Lactic acid as a platform chemical in the biobased economy: the role of chemocatalysis. *Energy Environ. Sci.* **6**, 1415–1442 (2013).
5. te Molder, T. D. J., Kersten, S. R. A., Lange, J.-P. & Ruiz, M. P. From woody biomass to ethylene glycol: inorganics removal boosts the yield. *Ind. Eng. Chem. Res.* **60**, 13515–13522 (2021).
6. Van Praet, S., Preegel, G., Rammal, F. & Sels, B. F. One-pot consecutive reductive amination synthesis of pharmaceuticals: from biobased glycolaldehyde to hydroxychloroquine. *ACS Sustain. Chem. Eng.* **10**, 6503–6508 (2022).
7. Schutyser, W. et al. Chemicals from lignin: an interplay of lignocellulose fractionation, depolymerisation, and upgrading. *Chem. Soc. Rev.* **47**, 852–908 (2018).
8. Sun, Z. et al. Complete lignocellulose conversion with integrated catalyst recycling yielding valuable aromatics and fuels. *Nat. Catal.* **1**, 82–92 (2018).
9. Liao, Y. et al. A sustainable wood biorefinery for low-carbon footprint chemicals production. *Science* **367**, 1385–1390 (2020).
10. Dusselier, M., Mascal, M. & Sels, B. F. in *Selective Catalysis for Renewable Feedstocks and Chemicals* (ed. Nicholas, K.) 1–40 (Springer Cham, 2014).
11. Lange, J.-P. Towards circular carbo-chemicals – the metamorphosis of petrochemicals. *Energy Environ. Sci.* **14**, 4358–4376 (2021).
12. Gao, C., Ma, C. & Xu, P. Biotechnological routes based on lactic acid production from biomass. *Biotechnol. Adv.* **29**, 930–939 (2011).
13. Araji, N. et al. Synthesis of maleic and fumaric acids from furfural in the presence of betaine hydrochloride and hydrogen peroxide. *Green Chem.* **19**, 98–101 (2017).
14. Yu, Q. et al. A sustainable system for maleic acid synthesis from biomass-derived sugar. *J. Chem. Technol. Biotechnol.* **95**, 751–757 (2020).
15. Kang, S., Fu, J. & Zhang, G. From lignocellulosic biomass to levulinic acid: a review on acid-catalyzed hydrolysis. *Renew. Sustain. Energy Rev.* **94**, 340–362 (2018).
16. Xu, W.-P. et al. Conversion of levulinic acid to valuable chemicals: a review. *J. Chem. Technol. Biotechnol.* **96**, 3009–3024 (2021).
17. Schwartz, T. J., Shanks, B. H. & Dumesic, J. A. Coupling chemical and biological catalysis: a flexible paradigm for producing biobased chemicals. *Curr. Opin. Biotechnol.* **38**, 54–62 (2016).
18. Shanks, B. H. & Keeling, P. L. Bioprivileged molecules: creating value from biomass. *Green Chem.* **19**, 3177–3185 (2017).
19. Shanks, B. H. & Broadbelt, L. J. A robust strategy for sustainable organic chemicals utilizing bioprivileged molecules. *ChemSusChem* **12**, 2970–2975 (2019).
20. Khalil, I., Quintens, G., Junkers, T. & Dusselier, M. Muconic acid isomers as platform chemicals and monomers in the biobased economy. *Green Chem.* **22**, 1517–1541 (2020).
21. Briou, B., Améduri, B. & Boutevin, B. Trends in the Diels–Alder reaction in polymer chemistry. *Chem. Soc. Rev.* **50**, 11055–11097 (2021).
22. Maniar, D. et al. Enzymatic synthesis of muconic acid-based polymers: trans, trans-dimethyl muconate and trans, β-dimethyl hydromuconate. *Polymers* **13**, 2498 (2021).
23. Zhang, H., Jiang, H., Zhang, Y., Zhang, N. & Xiong, R. Ferroelectric lithography in single-component organic enantiomorphic ferroelectrics. *Angew. Chem. Int. Ed.* **61**, e202200135 (2022).
24. Carter, P. et al. Bioenabled platform to access polyamides with built-in target properties. *J. Am. Chem. Soc.* **22**, 9548–9553 (2022).
25. He, J. et al. Zirconium phosphate supported copper catalyst for selective oxidation of phenol to *cis*, *cis*-muconic acid. *Appl. Catal. A* **664**, 119351 (2023).
26. Klein, B. C. et al. Economics and global warming potential of a commercial-scale delignifying biorefinery based on co-solvent enhanced lignocellulosic fractionation to produce alcohols, sustainable aviation fuels, and co-products from biomass. *Energy Environ. Sci.* **17**, 1202–1215 (2024).
27. Ling, C. et al. Muconic acid production from glucose and xylose in *Pseudomonas putida* via evolution and metabolic engineering. *Nat. Commun.* **13**, 4925 (2022).
28. Shiramizu, M. & Toste, F. D. Expanding the scope of biomass-derived chemicals through tandem reactions based on oxorhenium-catalyzed deoxydehydration. *Angew. Chem. Int. Ed.* **52**, 12905–12909 (2013).
29. Saraçi, E., Wang, L., Theopold, K. H. & Lobo, R. F. Bioderived muconates by cross-metathesis and their conversion into terephthalates. *ChemSusChem* **11**, 773–780 (2018).
30. Quintens, G., Vrijsen, J., Adriaensens, P., Vanderzande, D. & Junkers, T. Muconic acid esters as bio-based acrylate mimics. *Polym. Chem.* **10**, 5555–5563 (2019).
31. Carraher, J. M., Pfennig, T., Rao, R. G., Shanks, B. H. & Tessonnier, J. P. *cis*,*cis*-Muconic acid isomerization and catalytic conversion to biobased cyclic-C_6-1,4-diacid monomers. *Green Chem.* **19**, 3042–3050 (2017).
32. Lu, R. et al. Production of diethyl terephthalate from biomass-derived muconic acid. *Angew. Chem. Int. Ed.* **55**, 249–253 (2016).
33. Rammal, F., Gaumont, A. C. & Lakhdar, S. Metal-free visible-light-mediated aromatization of 1,2-dihydronaphthalenes. *Eur. J. Org. Chem.* **2020**, 1482–1485 (2020).
34. Carraher, J. M. et al. Solvent-driven isomerization of *cis*,*cis*-muconic acid for the production of specialty and performance-advantaged cyclic biobased monomers. *Green Chem.* **22**, 6444–6454 (2020).
35. Gopalakrishnan, D. K., Bhardwaj, S., Kumar, S., Karmakar, T. & Vaitla, J. Carbene-mediated stereoselective olefination of vinyl sulfoxonium ylides with diazo compounds and acetals. *Chem. Commun.* **60**, 3846–3849 (2024).
36. Grundmann, C. Zur kenntnis der oxydation von phenolen mit peressigsäure. *Ber. Dtsch. Chem. Ges.* **69**, 1755–1757 (1936).
37. Settle, A. E. et al. Iodine-catalyzed Isomerization of dimethyl muconate. *ChemSusChem* **11**, 1768–1780 (2018).
38. Frost, J. W., Miermont, A., Schweitzer, D. & Bui, V. Preparation of trans, trans muconic acid and trans, trans muconates. US patent US0314243 A1 (2010).
39. Bui, V., MacRae, D. & Schweitzer, D. Methods for producing isomers of muconic acid and muconate salts. US patent US0030215 (2013).
40. Tessonnier, J. P., Carraher, J. M., Pfennig, T. & Shanks, B. Isomerization of muconic acid. US patent US9957218 B2 (2018).
41. Khalil, I. et al. Solvent-driven isomerization of muconates in DMSO: reaction mechanism and process sustainability. *Green Chem.* **26**, 5852–5861 (2024).

42. Peeters, E. et al. Tandem reduction–reoxidation augments the catalytic activity of Sn-beta zeolites by redispersion and respeciation of SnO_2 clusters. *Chem. Mater.* **33**, 9366–9381 (2021).
43. Kerstens, D. et al. Fast and selective solvent-free branching of unsaturated fatty acids with hierarchical ZSM-5. *ACS Sustain. Chem. Eng.* **9**, 4357–4362 (2021).
44. Shah, M. A. et al. Catalytic amination of lactic acid using Ru–zeolites. *Dalton Trans.* **51**, 10773–10778 (2022).
45. Philippaerts, A. et al. Design of Ru–zeolites for hydrogen-free production of conjugated linoleic acids. *ChemSusChem* **4**, 757–767 (2011).
46. Yue, C. J., Liu, Y. & He, R. Olefins isomerization by hydride-complexes of ruthenium. *J. Mol. Catal. Chem.* **259**, 17–23 (2006).
47. Wang, A., Li, J. & Zhang, T. Heterogeneous single-atom catalysis. *Nat. Rev. Chem.* **2**, 65–81 (2018).
48. Ge, L. et al. Synergistic catalysis of Ru single-atoms and zeolite boosts high-efficiency hydrogen storage. *Appl. Catal. B* **319**, 121958 (2022).
49. Matthiesen, J. E., Carraher, J. M., Vasiliu, M., Dixon, D. A. & Tessonnier, J. P. Electrochemical conversion of muconic acid to biobased diacid monomers. *ACS Sustain. Chem. Eng.* **4**, 3575–3585 (2016).
50. Qiu, J.-Z. et al. Pure siliceous zeolite-supported Ru single-atom active sites for ammonia synthesis. *Chem. Mater.* **31**, 9413–9421 (2019).
51. Tekin, K., Hao, N., Karagoz, S. & Ragauskas, A. J. Ethanol: a promising green solvent for the deconstruction of lignocellulose. *ChemSusChem* **11**, 3559–3575 (2018).
52. Yang, H. et al. Isolated single-atom ruthenium anchored on beta zeolite as an efficient heterogeneous catalyst for styrene epoxidation. *ChemNanoMat* **6**, 1647–1651 (2020).
53. Sun, R. et al. Heterogeneous catalysts for CO_2 hydrogenation to formic acid/formate: from nanoscale to single atom. *Energy Environ. Sci.* **14**, 1247–1285 (2021).
54. Ghoreishian, S. M., Shariati, K., Huh, Y. S. & Lauterbach, J. Recent advances in ammonia synthesis over ruthenium single-atom-embedded catalysts: a focused review. *Chem. Eng. J.* **467**, 143533 (2023).
55. Mon, M. et al. Stabilized $Ru[(H_2O)_6]^{3+}$ in confined spaces (MOFs and zeolites) catalyzes the imination of primary alcohols under atmospheric conditions with wide scope. *ACS Catal.* **8**, 1 0401–10406 (2018).
56. Wang, D. & Astruc, D. The golden age of transfer hydrogenation. *Chem. Rev.* **115**, 6621–6686 (2015).
57. Capeletti, M. R., Balzano, L., de la Puente, G., Laborde, M. & Sedran, U. Synthesis of acetal (1,1-diethoxyethane) from ethanol and acetaldehyde over acidic catalysts. *Appl. Catal. A* **198**, L1–L4 (2000).
58. Hao, W. et al. Ru-catalyzed enantioselective hydrogenation of 2-pyridyl-substituted alkenes and substrate-mediated H/D exchange. *ACS Catal.* **12**, 1150–1160 (2022).
59. Kita, Y., Kuwabara, M., Yamadera, S., Kamata, K. & Hara, M. Effects of ruthenium hydride species on primary amine synthesis by direct amination of alcohols over a heterogeneous Ru catalyst. *Chem. Sci.* **11**, 9884–9890 (2020).
60. Wachs, I. E. & Bañares, M. A. (eds) *Springer Handbook of Advanced Catalyst Characterization* (Springer Cham, 2023).
61. Wang, X. & Andrews, L. Infrared spectra and theoretical calculations for Fe, Ru, and Os metal hydrides and dihydrogen complexes. *J. Phys. Chem. A* **113**, 551–563 (2009).
62. Settle, A. E. et al. Heterogeneous Diels–Alder catalysis for biomass-derived aromatic compounds. *Green Chem.* **19**, 3468–3492 (2017).
63. Shang, Y., Xu, X., Gao, B., Wang, S. & Duan, X. Single-atom catalysis in advanced oxidation processes for environmental remediation. *Chem. Soc. Rev.* **50**, 5281–5322 (2021).
64. Devos, J. et al. Engineering low-temperature ozone activation of zeolites: process specifics, possible mechanisms and hybrid activation methods. *Chem. Eng. J.* **431**, 133862 (2022).
65. Zavala-Sanchez, L., Khalil, I., Oliviero, L., Paul, J. & Maugé, F. Structure and quantification of edge sites of WS_2/Al_2O_3 catalysts coupling IR/CO spectroscopy and DFT calculations. *ChemCatChem* **12**, 2066–2076 (2020).
66. Emeis, C. A. Determination of integrated molar extinction coefficients for infrared absorption bands of pyridine adsorbed on solid acid catalysts. *J. Catal.* **141**, 347–354 (1993).
67. Devos, J., Robijns, S., Van Goethem, C., Khalil, I. & Dusselier, M. Interzeolite conversion and the role of aluminum: toward generic principles of acid site genesis and distributions in ZSM-5 and SSZ-13. *Chem. Mater.* **33**, 2516–2531 (2021).
68. Ravel, B. & Newville, M. ATHENA, ARTEMIS, HEPHAESTUS: data analysis for X-ray absorption spectroscopy using IFEFFIT. *J. Synchrotron Radiat.* **12**, 537–541 (2005).
69. te Velde, G. et al. Chemistry with ADF. *J. Comput. Chem.* **22**, 931–967 (2001).
70. Martini, A. et al. PyFitIt: the software for quantitative analysis of XANES spectra using machine-learning algorithms. *Comput. Phys. Commun.* **250**, 107064 (2020).

Acknowledgements

We thank the FWO Foundation for the projects and grants 1260321N (I.K.), 12A3M24N (I.K.), G0F2320N (K.J. and D.D.V.), AKUL13/19 and I000920N (M.T.B. and M.D.). Part of this work was performed in the framework of the Catalisti cluster SBO project SPICY ('Sugar-based chemicals and Polymers through Innovative Chemocatalysis and engineered Yeast'), with the financial support of VLAIO (Flemish Agency for Innovation and Entrepreneurship; HBC.2017.0597 (I.K. and M.D.)). We thank the European Synchrotron Radiation Facility for providing the beamtime (proposal MA-4443) at the BM23 beamline, and K. Lomachenko for the professional support (A.B.). We thank the European Research Council (ERC) for the ERC Consolidator Grants, no. 815128 REALNANO and no. 823717 ESTEEM3 (D.A.E. and S.B.), under the European Union's Horizon 2020 research and innovation programme. We thank the ERC for ERC Starting Grant no. 948449 Z-EURECA (M.T.B. and M.D.), under the European Union's Horizon 2020 research and innovation programme.

Author contributions

I.K. performed the conceptualization, experimental investigation, data analysis, funding acquisition, writing, reviewing and editing. M.G.R., K.J., A.B. and D.A.E. performed the experimental investigation, design of the methodology, writing, reviewing and editing. S.R., T.D. and M.T.B. characterized the catalytic materials and helped in writing, reviewing and editing. S.B. performed data analysis and edited the paper. D.D.V. contributed to the conceptualization of experiments, the data analysis and the paper editing. M.D. supervised the project, performed the conceptualization and data visualization, acquired resources and funds and reviewed and edited the paper.

Competing interests

The authors declare no competing interests.

Additional information

Supplementary information The online version contains supplementary material available at https://doi.org/10.1038/s41929-024-01205-5.

Correspondence and requests for materials should be addressed to Michiel Dusselier.

Peer review information *Nature Catalysis* thanks Jean-Philippe Tessonnier, Jie Xu and the other, anonymous, reviewer(s) for their contribution to the peer review of this work.